Multiple layer kernel extreme learning machine modeling and eugenics genetic sparrow search algorithm for the state of health estimation of lithium-ion batteries.

LI, Y., WANG, S., CHEN, L., QI, C. and FERNANDEZ, C.

2023

Multiple layer kernel extreme learning machine modeling and eugenics genetic sparrow search algorithm for the state of health estimation of lithium-ion batteries

Yang Li[a], Shunli Wang[a]*, Lei Chen[a], Chuangshi Qi[a], Carlos Fernandez[b]

[a]School of Information Engineering, Southwest University of Science and Technology, Mianyang 621010, China; [b]Robert Gordon Univ, Sch Pharm & Life Sci, Aberdeen, Scotland.

Abstract: High precision state of health (SOH) estimation of lithium-ion batteries (LIBs) is a research hotspot in battery management system (BMS). To achieve this goal, an improved integrated algorithm based on multiple layer kernel extreme learning machine (ML-KELM) and eugenics genetic sparrow search (EGSS) algorithm is proposed to estimate the SOH of LIBs. First, a kernel version of ML-ELM model is constructed for initial SOH estimation of LIBs. The kernel function parameters are used to simulate sparrow foraging and anti-predatory behaviors, and the parameter optimization process is completed in the proposed EGSS algorithm by iteratively updating the position of sparrows to improve SOH prediction accuracy and model stability. The cycle data of different specifications of LIB units are processed to construct the high-dimensional health feature (HF) dataset and the low-dimensional fusion feature (FF) dataset, and each version of ML-ELM network is trained and tested separately. The numerical analysis of the prediction results shows that the best root mean square error (RMSE) of the comprehensive algorithm for SOH estimation is limited within 0.29%. The results of the multi-indicator comparison show that the proposed algorithm can track the true value stably and accurately with satisfactory high accuracy and strong robustness.

Key words: State of health; Lithium-ion batteries; Multiple layer kernel extreme learning machine; Eugenics genetic sparrow search algorithm; Fusion features; Multi-indicator comparison

***Corresponding author**: Shun-Li Wang. E-mail address: 497420789@qq.com.

1. Introduction

The advantages of high energy density, long service life, and low environmental pollution make LIBs widely used in new energy vehicles, special robots, aerospace, and other fields [1, 2]. However, there are a series of safety problems caused by improper monitoring and management of LIBs [3-5]. Therefore, it is very important for the development of BMS and new energy vehicles to estimate the status of LIBs [6]. Accurate SOH value is the key prerequisite for the safe charging and discharging, service life prediction, and real-time power management of group batteries. The different working conditions of LIBs will lead to great differences in the internal chemical reaction rate of the batteries [7, 8]. Besides, the LIBs have a strong nonlinearity, which also causes errors in the measured values of sensors and increases the difficulty of accurate monitoring and prediction of the battery state [9-11].

The SOH estimation methods of LIBs mainly include model-based [12-14] and data-driven [15-17] estimation methods. The model-based approach is based on the mechanism of battery internal performance degradation, establishing a physical model that can reflect the battery performance degradation characteristics, and then completing the SOH estimation of LIBs through model parameter identification, in which the electrochemical model [18] needs to be modeled independently based on different types of battery materials, structures, etc. The model is often complex, computationally intensive and does not have generalization. The equivalent circuit model (ECM) [19, 20] simulates the simplified electrochemical reactions inside the battery with electronic components, which is easy to implement but has poor accuracy, and it is often combined with filtering methods. Qiu et al. [21] apply the cuckoo search algorithm to optimize the particle filter algorithm, and Bi et al. [22] determine the parameters of the battery model by genetic resampling particle filtering method. Under such conditions, the prediction accuracy of the model is significantly improved.

The data-driven estimation method does not need to analyze the internal mechanism of the LIBs [23].

The battery operation process data (voltage, current, temperature, etc.) are collected and analyzed, from which the battery degradation information and rules are mined, and the SOH of LIBs is estimated using intelligent algorithms [24, 25]. Through learning the internal relationship of samples in the training dataset, the neural network continuously makes predictions and adjusts its structural parameters according to errors, making the model perform well under the test dataset [26, 27]. Patil et al. [28] combine the classification and regression stages of support vector machine (SVM) to extract key features from the curves of battery aging experimental data to improve the SOH prediction accuracy and computational efficiency of lithium-ion batteries. Li et al. [29] employed a modified long short-term memory (LSTM) neural network to get the SOH results using historical capacity and a significant amount of battery offline data as input and future capacity and offline capacity as output.

Extreme learning machine (ELM) [30-32] is proposed with the idea of reducing parameter setting and selection through a stochastic mechanism, and has been rapidly developed as it shows faster learning and better generalization compared to back propagation (BP) algorithm. The architecture of ML-ELM is first defined by Kasun et al [33], who give the complete training procedure for this hierarchical information architecture. Given that ML-ELM integrates the advantages of developing ELM, it has been widely used in many fields. Nowadays, multidimensional health features derived from life-cycle data are frequently used as input in data-driven SOH prediction methodologies [34, 35]. When extracting the effective information layer by layer, the ML-ELM will be limited by the high-dimensional input, which causes a problem with prediction accuracy and increases the computational cost. Furthermore, the parameters of each hidden layer of ML-ELM are generated at random, resulting in significantly different prediction results. In addition, the reconstruction error caused by layer-by-layer pseudo-inverse operation will accumulate layer by layer and affect the model performance [36, 37].

In this paper, a high-precision SOH prediction method for lithium-ion batteries integrating multiple

layer kernel extreme learning machine (ML-KELM) modeling and eugenics genetic sparrow search (EGSS) algorithm is proposed to address the aforementioned issues. Firstly, a kernel version of ML-ELM is established, and then the sparrow search algorithm is optimized based on genetic ideas, followed by the construction of a traditional high-dimensional feature dataset and a low-dimensional fused feature dataset for model training and testing. Finally, the prediction results are numerically evaluated under four evaluation indicators to demonstrate the accuracy advantages and robustness of the proposed algorithm. The main contributions are as follows.

(1) In ML-ELM network, there are problems such as low prediction accuracy and poor stability caused by the accumulation of reconstruction errors and the random initialization of parameters. The radial basis function (RBF) is used to replace the random mapping mechanism of the ML-ELM network, which significantly enhances the prediction stability of the algorithm.

(2) Aiming at the problem that traditional SS algorithms are prone to fall into local optima, the global optimal solution of the previous generation and the average fitness of some excellent individuals are introduced into the position update mode of contemporary sparrows responsible for foraging, while optimizing the position update mode of sparrows responsible for guarding, making the improved SS algorithm have stronger parameter optimization capabilities.

(3) For SOH estimation, the prediction accuracy of ML-ELM is limited when dealing with a large amount of high-dimensional input data. In order to improve the performance of the algorithm, the highly correlated health features extracted from the aging data are fused according to the weight and used as network input to reduce the data dimension and noise interference caused by a large number of original data, so that the network has stronger stability and generalization ability.

(4) The integrated algorithm is tested on two different dimensional feature datasets constructed, and the numerical results of four evaluation indicators show that the algorithm has the advantages of high

accuracy and strong robustness.

The paper is organized as follows: Section 2 introduces data sets and data processing. Section 3 describes the structure and operation of ML-KELM, as well as the mathematical equation of the SS algorithm, which is based on genetic idea optimization. Section 4 analyzes the experimental results from multiple dimensions. Section 5 summarizes the paper.

2. Data description

SOH reflects the current health status of LIBs, and its value represents the current capacity of the battery as a percentage of the rated capacity. Therefore, the state of health of LIBs is often characterized in the form of capacity, as defined in Eq. (1).

$$SOH_t = \frac{C_t}{C_N} \cdot 100\% \tag{1}$$

In Eq. (1), C_t denotes the capacity at time t, C_N denotes the initial capacity at the beginning of aging, and SOH_t denotes the SOH at time t. In this research, the EGSS-ML-KELM algorithm is verified on public datasets 1 (from NASA Ames Prognostics Center of Excellence) [38, 39] and 2 (from the Center for Advanced Life Cycle Engineering) [40, 41] that are widely used for life and capacity testing of LIBs based on data-driven. A total of 7 LIBs units are selected from the two datasets. The capacity attenuation curve of LIBs obtained from the discharge measurements is shown in Fig. 1.

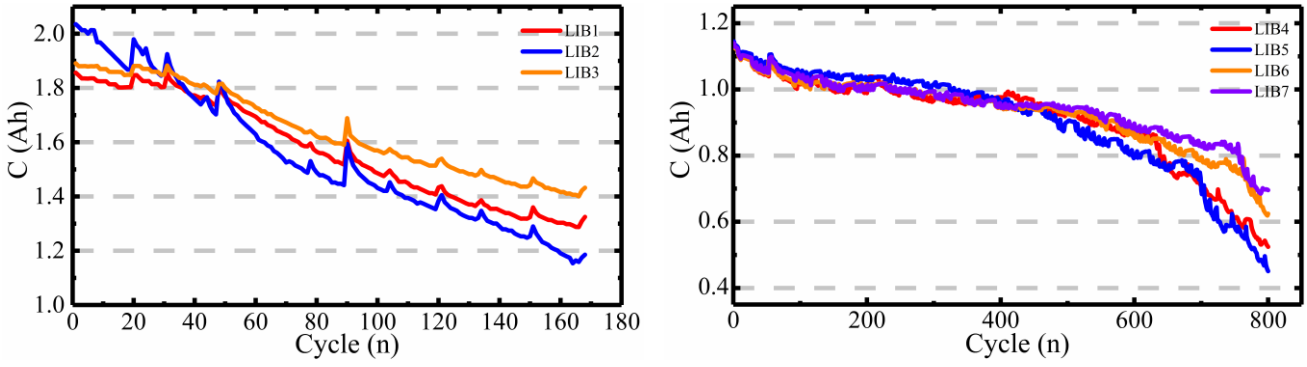

(a) Capacity attenuation curve of LIBs in dataset 1

(b) Capacity attenuation curve of LIBs in dataset 2

Fig. 1 Capacity attenuation curve of LIBs

In Fig. 1, all LIBs are charged in constant current (CC) mode until the battery voltage reaches the upper cut-off voltage, and then continue charging in constant voltage (CV) mode until the charging current drops below 20mA. During the discharge phase, all LIBs are discharged at a constant current until the battery voltage drops to the lower limit cut-off voltage, which is the end of a complete cycle. The specifications of the selected LIBs are shown in Tab. 1.

Tab. 1 Specification of the selected LIBs

Battery characteristic	Specification						
	Dataset 1			Dataset 2			
	LIB1	LIB2	LIB3	LIB4	LIB5	LIB6	LIB7
Cell type	Cylindrical			Prismatic			
Nominal capacity	2Ah			1.1Ah			
Charge current	1.5A			0.55A			
Discharge current	2A			1.1A			
Upper cut-off voltage	4.2V			4.2V			
Lower cut-off voltage	2.7V	2.5V	2.2V	2.7V			

Among them, the data of dataset 1 is collected from the customized battery prediction test bench, which mainly includes programmable DC electronic load and power supply, thermocouple sensor, voltmeter, ammeter, electrochemical impedance spectrum and data collector based on PXI chassis. The impedance measurement is conducted through the frequency scanning of electrochemical impedance spectrum from 0.1 Hz to 5 kHz to measure the battery capacity. The cycling of the battery in dataset 2 is completed by conducting multiple charge and discharge tests using the Arbin BT2000 battery testing system at room temperature. The Coulomb counting method is used to estimate the capacity of the test

battery, as a complete charge-discharge cycle is conducted. For the raw measurement data (voltage, current, temperature, etc.) in the dataset, there are often abnormal points or noises, which will lead to large prediction errors if these data are directly used as neural network input. Therefore, it is necessary to preprocess the original data. The parameter change curve in the process of life degradation is extracted from two sets of datasets, and some examples are shown in Fig. 2.

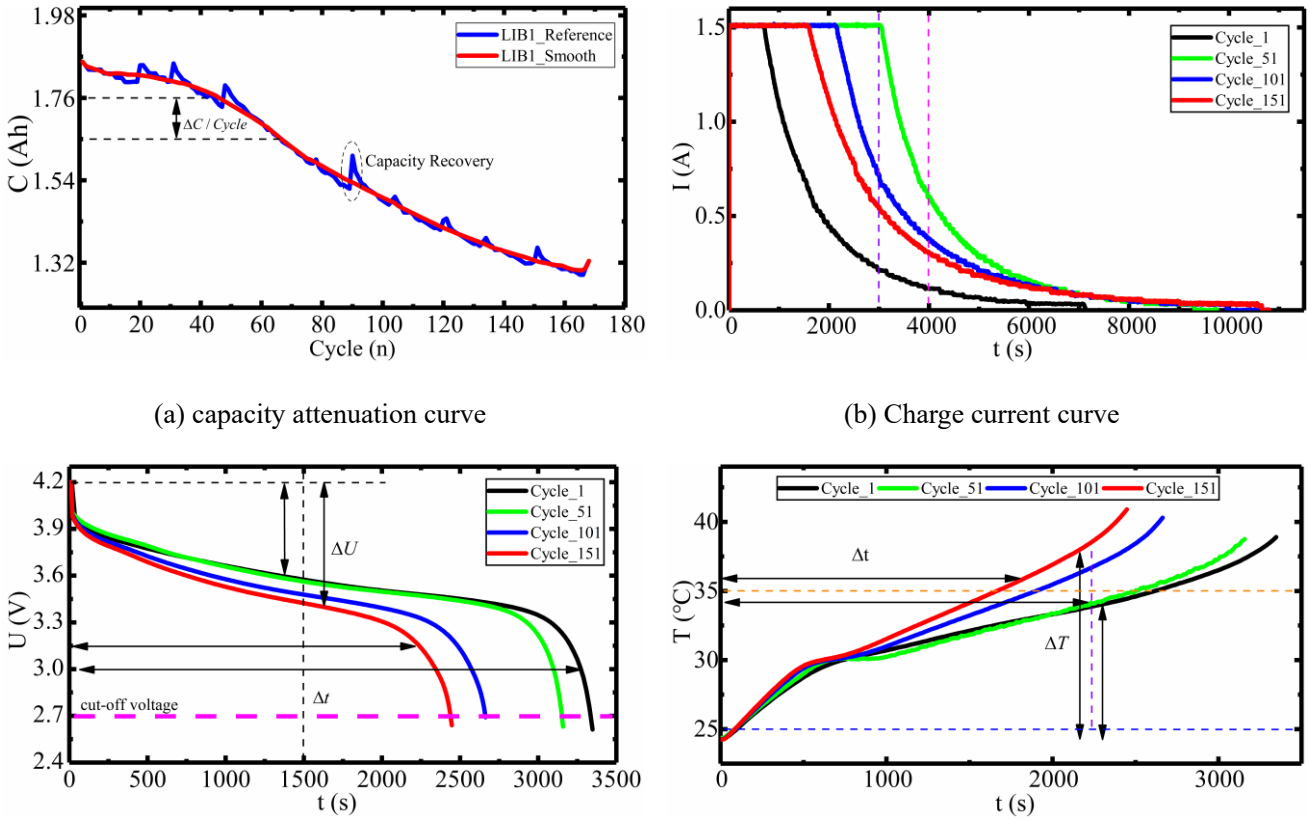

(a) capacity attenuation curve

(b) Charge current curve

(c) Discharge voltage curve

(d) Temperature curve in discharge stage

Fig. 2 Characteristic curve of raw data

The data outliers due to the capacity recovery effect will cause the final results to be abnormal. Smooth function shown in Eq. (2) is used for processing to improve the prediction accuracy of the algorithm, and the optimized capacity attenuation curve is shown in Fig. 2(a).

$$\begin{cases} y(1) = c(1) \\ y(2) = \dfrac{1}{3}(c(1) + c(2) + c(3)) \\ y(i) = \dfrac{1}{5}\big(c(i-2) + c(i-1) + c(i) + c(i+1) + c(i+2)\big) \quad i = 3,4,5,\ldots \end{cases} \tag{2}$$

In Eq. (2), y denotes the capacity data after smoothing, c denotes the raw capacity data, and i denotes a positive integer greater than or equal to 3. That is, average moving filtering is performed on the capacity data, and the moving step is set to 5.

The aging of LIBs is a long-term process. In data-driven algorithms for estimating the capacity of LIBs, health features highly related to the life decay of lithium-ion batteries are usually used as network inputs rather than directly using these large amounts of raw data. Nevertheless, health features are often defined and constructed by researchers, which leads to higher dimensions of input data of the network, and increases computational complexity and estimation efficiency. In this research, the extracted multiple health features are fused through the idea of weighting, which greatly reduces the dimensions of data while retaining effective information. The specific process is shown in Fig. 3.

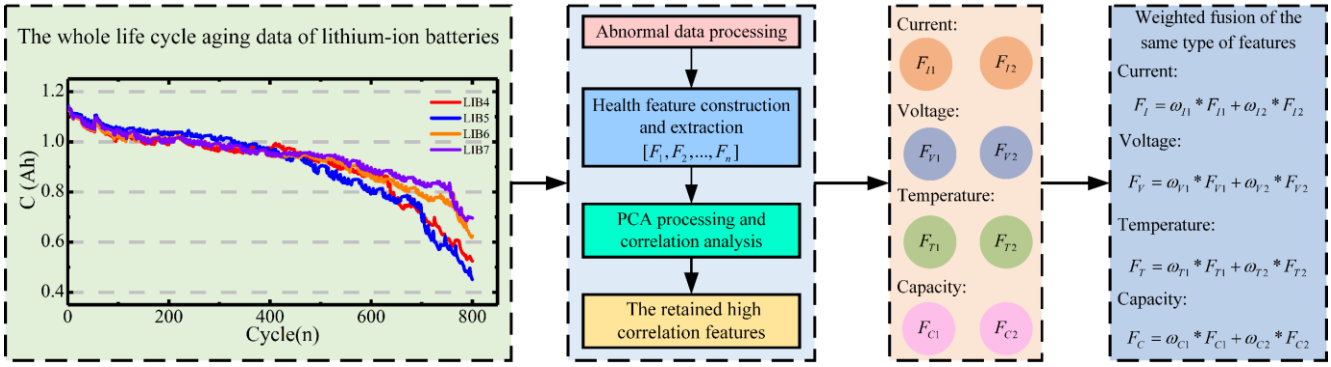

Fig. 3 Schematic diagram of weighted fusion features

In Fig. 3, the current, voltage and temperature change curves of each cycle are extracted from the two datasets, and the curve change rate, equal voltage drop discharge time, unit time capacity change, etc. are selected to construct multiple health features. In order to screen out features that contain duplicate information, the constructed features are processed using principal component analysis (PCA) as shown in Tab. 2 and transformed into linearly independent features.

Tab. 2 The steps for the PCA method

Step 1: Form the original data into a matrix X of $n * m$.

Step 2: Each element of matrix X minus the mean of the row in which it is located.

Step 3: Calculate the covariance matrix C ($C = \frac{1}{m}XX^T$) of matrix X.

Step 4: Calculate the eigenvalues and corresponding eigenvectors of matrix C.

Step 5: The corresponding eigenvectors are arranged in rows according to the magnitude of the eigenvalues to form a matrix, and the first k rows are taken to form a matrix P.

Step 6: Calculate the objective matrix Y ($Y = PX$).

The constructed health features are processed by the above steps to obtain k mutually independent health features. Then, the correlation analysis of the obtained k features is performed according to the Pearson correlation coefficient shown in Eq. (3).

$$\rho(x,y) = \frac{Con(x,y)}{\sigma(x)\sigma(y)} = \frac{\sum_{i=1}^{n}(x_i - \bar{x})(y_i - \bar{y})}{\sqrt{\sum_{i=1}^{n}(x_i - \bar{x})^2}\sqrt{\sum_{i=1}^{n}(y_i - \bar{y})^2}} \tag{3}$$

In Eq. (3), $Con(x,y)$ is the covariance of variables x and y, σ is the standard deviation, n is the length of the variable, and $\bar{x}$ and $\bar{y}$ are the means of x and y.

Then, based on the overall correlation coefficient of each feature, the two features with the highest correlation with LIBs aging are selected from four categories of current, voltage, temperature, and capacity respectively. The specific definition of retained features are shown in Tab. 3.

Tab. 3 Definition of retained high correlation features

Features	Definition
F_{I1}	The time of the constant current charging stage.
F_{I2}	The area enclosed by the current curve of each cycle and the x-axis in charge stage.
F_{V1}	The time it takes for the voltage curve to decrease to specified value in discharge stage.
F_{V2}	The area enclosed by the voltage curve of each cycle and the x-axis in discharge stage.
F_{T1}	The time it takes for the temperature curve to rise to specified value in discharge stage.

F_{T2}	The area enclosed by the temperature curve of and the x-axis in discharge stage.
F_{C1}	The decay rate of the capacity curve after smoothing in steps of 5 cycles.
F_{C2}	The area enclosed by the capacity curve and the x-axis in steps of 5 cycles.

Based on the retained health features in Tab. 3, construct the traditional high-dimensional feature dataset. Then, these features are weighted and fused to construct a low-dimensional fused feature dataset. The overall correlation coefficients of the above retained features are shown in Tab. 4.

Tab. 4 Overall correlation coefficient of retained features

Battery	Feature correlation coefficient (ρ)							
	F_{I1}	F_{I2}	F_{V1}	F_{V2}	F_{T1}	F_{T2}	F_{C1}	F_{C2}
LIB1	0.8284	0.7878	0.7881	0.7586	0.8027	0.7883	0.9521	0.8987
LIB2	0.7704	0.7720	0.7723	0.7518	0.7515	0.7487	0.9156	0.9043
LIB3	0.8729	0.8088	0.8094	0.7448	0.8327	0.8632	0.9212	0.9330
LIB4	0.8829	0.8747	0.8692	0.8850	0.8202	0.8949	0.9201	0.9470
LIB5	0.9101	0.8916	0.8262	0.8556	0.8037	0.8825	0.9745	0.8780
LIB6	0.8954	0.8828	0.9196	0.8531	0.8538	0.9167	0.9709	0.8877
LIB7	0.86272	0.9082	0.8321	0.8095	0.7917	0.8908	0.9304	0.9487

Then, based on the overall correlation coefficient ρ in Tab. 4, the features are weighted and fused according to the principle shown in Eq. (4).

$$\begin{cases} \omega_{ji} = \dfrac{\dfrac{1}{\rho_{ji}}}{\sum_{i=1}^{2}\dfrac{1}{\rho_{ji}}} \\ F_j = \sum_{i=1}^{2} \omega_{ji} * F_{ji} \end{cases} \tag{4}$$

In Eq. (4), $\{i = 1, 2;\ j = I, V, T, C\}$, ω_{ji} denotes the weight of each feature, ρ_{ji} denotes the

correlation coefficient of each feature, F_j denotes the fusion feature, and F_{ji} denotes each feature sequence.. The seven LIB cells life cycle data are processed identically to obtain the corresponding health feature dataset and the corresponding fusion feature dataset.

3. Methodology

3.1 The kernel version of ML-ELM modeling

Automatic encoder (AE) is a simple and efficient calculation method. ELM-AE combines ELM and AE as an unsupervised neural network model, whose output is equal to the input. The learning process of ML-ELM is completed by stacking multiple ELM-AEs to extract effective information hierarchically. To reduce the instability of prediction results caused by random initialization of ML-ELM network parameters (weights, thresholds, etc.) and the reconstruction errors accumulated layer by layer, a kernel learning mechanism is introduced to replace the structural parameters of each layer by a kernel function matrix, and the eugenics genetics sparrow search algorithm introduced in Section 3.2 is used to perform extreme value seeking on the kernel function parameters to achieve high accuracy SOH prediction of LIBs. The principle structure of ML-KELM is shown in Fig. 4.

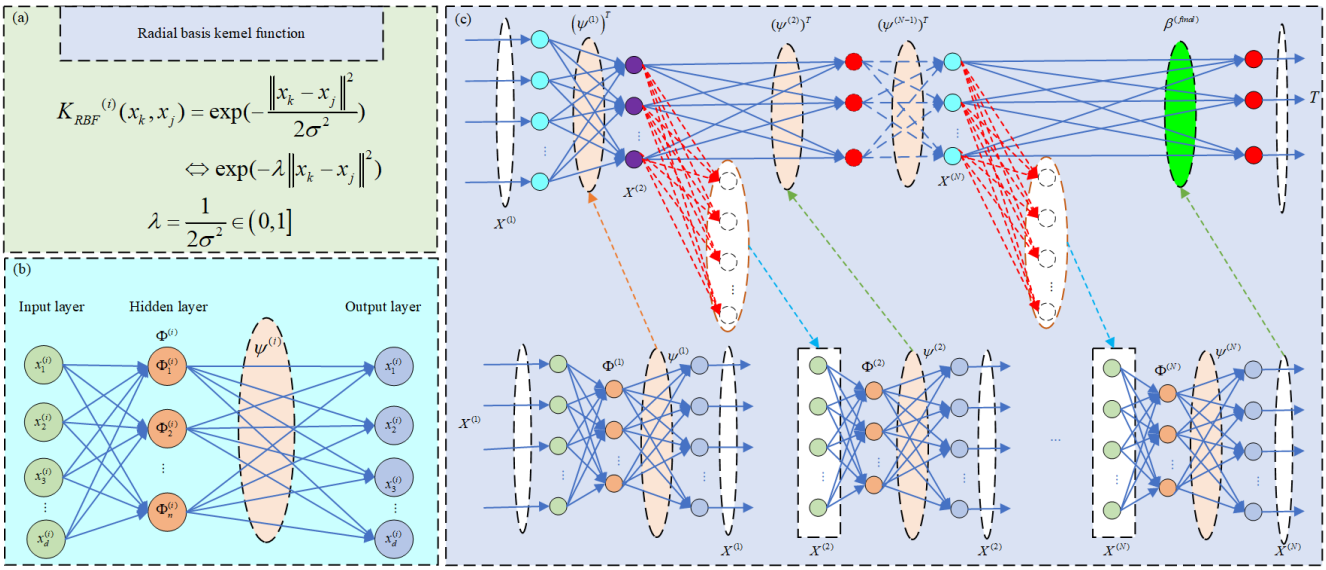

Fig. 4. The ML-KELM network topology. (a) The RBF kernel function. (b) The i_{th} KELM-AE of ML-ELM. (c) The

ML-KELM structure diagram

In Fig. 4(c), multiple ELM-AE stack structure is used to extract sample features of input data layer by layer without supervision to complete the learning process, while a single ELM is used as the final supervised regression layer to complete the prediction output. Therefore, the kernel version of ELM-AE shown in Fig. 4(b) needs to be built first.

For a dataset containing n pieces of training samples, assume that it can be represented as $\aleph = \{(X_k, T_k)|k = 1,2,\dots,n\}$, where $X_k = [x_{k1}, x_{k2}, \dots, x_{kd}]$, $T_k = [t_{k1}, t_{k2}, \dots, t_{kc}]$. Then for hidden layer node h_m (input weight is a_m and bias is b_m), its output weight $\beta_m = [\beta_{m1}, \beta_{m2}, \dots, \beta_{mc}]^T$ and output matrix $h_m(a_m, b_m, x) = a_m x + b_m$. For all hidden layer nodes, the output matrix can be expressed as Eq. (5).

$$\boldsymbol{H} = \begin{bmatrix} h_1(a_1, b_1, x_1) & \cdots & h_L(a_L, b_L, x_1) \\ \vdots & \ddots & \vdots \\ h_1(a_1, b_1, x_n) & \cdots & h_L(a_L, b_L, x_n) \end{bmatrix} \tag{5}$$

And the corresponding weight matrix and target matrix can be expressed as Eq. (6).

$$\boldsymbol{\beta} = \begin{bmatrix} \beta_1^T \\ \vdots \\ \beta_L^T \end{bmatrix}, \ \boldsymbol{T} = \begin{bmatrix} t_{11} & \cdots & t_{1c} \\ \vdots & \ddots & \vdots \\ t_{n1} & \cdots & t_{nc} \end{bmatrix} \tag{6}$$

Then, an ELM-AE model can be expressed in matrix form as Eq. (7).

$$\boldsymbol{H\beta} = \boldsymbol{T} \tag{7}$$

In order to prevent the prediction results from over fitting and limit complexity of the model, the regularization coefficient C is introduced, so an ELM-AE model can be expressed as Eq. (8).

$$f_{ELM-AE}(\boldsymbol{x}) = \boldsymbol{h}(\boldsymbol{x})\boldsymbol{H}^{\boldsymbol{T}} \left(\frac{I}{C} + \boldsymbol{H}\boldsymbol{H}^{\boldsymbol{T}}\right)^{-1} \boldsymbol{T} \tag{8}$$

To reduce the impact of random generation of input weights $\boldsymbol{a}$ and bias $\boldsymbol{b}$ in Eq. (5), replace $\boldsymbol{H}\boldsymbol{H}^{\boldsymbol{T}}$ in Eq. (8) with the kernel function matrix $\boldsymbol{\Phi}$ shown in Eq. (9).

$$\boldsymbol{\Phi}(x_k, x_j) = \exp(-\lambda \|x_k - x_j\|^2) \tag{9}$$

In Eq. (9), $\boldsymbol{\Phi}(x_k, x_j)$ is the radial basis function with single parameter λ. Then, the kernel version

of ELM-AE model can be expressed as Eq. (10).

$$f_{KELM-AE}(\boldsymbol{x}) = \boldsymbol{h}(x)\boldsymbol{H}^{\boldsymbol{T}}\left(\frac{I}{C} + \boldsymbol{\Phi}\right)^{-1}\boldsymbol{T} \tag{10}$$

In Eq. (10), $\boldsymbol{h}(\boldsymbol{x})\boldsymbol{H}^{\boldsymbol{T}} = \begin{bmatrix}\boldsymbol{\Phi}(x, x_1)\\ \vdots \\ \boldsymbol{\Phi}(x, x_n)\end{bmatrix}$, which means that the hidden layer becomes a kernel matrix $\boldsymbol{\Phi}$. Then, the kernel version of ELM-AE is obtained, where the input matrix $\boldsymbol{X}^{(i)} = [x_1^{(i)}, \dots, x_d^{(i)}]$, the kernel matrix $\boldsymbol{\Phi}^{(i)} = [\Phi_1^{(i)}, \dots, \Phi_n^{(i)}]$, the transformation matrix $\boldsymbol{\psi}^{(i)} = [\beta_1^{(i)}, \dots, \beta_n^{(i)}]$. Under this premise, by building the ML-KELM structure shown in Fig. 4(c), the prediction results can be obtained through the following data conversion process.

Assume that the input matrix is $\boldsymbol{X}^{(1)}$, output matrix is $\boldsymbol{T}$, kernel parameter of all hidden layers is λ_i, regularization coefficient of all layers is C_i, the number of KELM-AE is *N*, and the activation function is g_i. Similarly, for the i_{th} ELM-AE ($i = 2,3, \dots N$), Eq. (11) can be obtained by replacing $\boldsymbol{\beta}$ with $\boldsymbol{\Omega}^{(i)}$ and $\boldsymbol{T}$ with $\boldsymbol{X}^{(i)}$ in Eq. (7).

$$\boldsymbol{H}^{(i)}\boldsymbol{\Omega}^{(i)} = \boldsymbol{X}^{(i)} \tag{11}$$

Then, through the pseudo-inverse matrix of the output matrix $\boldsymbol{H}^{(i)}$, the transformation matrix $\boldsymbol{\Omega}^{(i)}$ can be obtained as shown in Eq. (12).

$$\boldsymbol{\Omega}^{(i)} = \left(\boldsymbol{H}^{(i)}\right)^{\boldsymbol{T}}\left(\frac{I}{C} + \boldsymbol{H}^{(i)}\left(\boldsymbol{H}^{(i)}\right)^{\boldsymbol{T}}\right)^{-1}\boldsymbol{X}^{(i)} \tag{12}$$

When the iterative calculation of each KELM-AE is completed, it indicates the end of the learning process. At this time, the output of the last KELM-AE can be expressed as Eq. (13).

$$\boldsymbol{X}^{(N)} = g\left(\boldsymbol{X}^{(N)}(\boldsymbol{\Omega}^{(N)})^{\boldsymbol{T}}\right) \tag{13}$$

In Eq. (13), $\boldsymbol{X}^{(N)}$ is not only the output of the last KELM-AE, but also the input of the single ELM used for regression. Therefore, the final output can be expressed as Eq. (14).

$$\boldsymbol{X}^{(N)}\boldsymbol{\beta}^{\text{final}} = \boldsymbol{T} \tag{14}$$

In Eq. (14), $\boldsymbol{\beta}^{\text{final}}$ is the output weight matrix of the ELM, which can be calculated by Eq. (15).

$$\boldsymbol{\beta}^{\text{final}} = \boldsymbol{X}^{(N)}\left(\frac{I}{C} + \boldsymbol{X}^{(N)}\left(\boldsymbol{X}^{(N)}\right)^{\boldsymbol{T}}\right)^{-1}\boldsymbol{T} \tag{15}$$

In ML-ELM, ELM-AE uses pseudoinverse to solve the transformation matrix $\boldsymbol{\Omega}^{(i)}$ corresponding to each input matrix $\boldsymbol{X}^{(i)}$, so each layer will produce reconstruction error, while ML-ELM will minimize the reconstruction error of each ELM-AE, and the reconstruction error will accumulate and propagate layer by layer in the process of determining that each $\boldsymbol{\Omega}^{(i)}$ is used for subsequent iterations, which will produce larger reconstruction error compared with the exact inverse. In addition, the hidden layer nodes $\boldsymbol{h}_i$ of each ELM-AE in ML-ELM need to be set manually, and the problem of model instability caused by random generation of input weight $\boldsymbol{a}_i$ and bias $\boldsymbol{b}_i$ cannot be ignored.

Inspired by the fact that the kernel learning method can perform well without adjusting parameters $\boldsymbol{h}_i$, $\boldsymbol{a}_i$, and $\boldsymbol{b}_i$, the $\boldsymbol{HH}^{\boldsymbol{T}}$ matrix of each ELM-AE in ML-ELM is replaced by the corresponding kernel function matrix $\boldsymbol{\Phi}$, as shown in Eq. (10), to obtain ML-KELM. In this case, the burden of setting $\boldsymbol{h}_i$ of each hidden layer and the unstable influence caused by randomly generating $\boldsymbol{a}_i$ and $\boldsymbol{b}_i$ are eliminated. Besides, under the invertible kernel matrix $\boldsymbol{\Phi}$, the transformation matrix $\boldsymbol{\Omega}^{(i)}$ can be calculated by exact inversion rather than pseudo inversion, which greatly reduces the reconstruction error.

In Fig. 4(c), the hidden layer of each KELM-AE is replaced by a kernel function matrix $\boldsymbol{\Phi}^{(i)}$, so that under the fixed kernel parameter $\boldsymbol{\lambda}_i$, ML-KELM can complete the training process at one time without spending too much time to explore the optimal combination of $\boldsymbol{h}_i$, $\boldsymbol{a}_i$, and $\boldsymbol{b}_i$. However, the performance of the kernel function often depends directly on its parameters. Therefore, how to determine the optimal value of each kernel parameter $\boldsymbol{\lambda}_i$ is another problem that needs to be solved urgently. In this research, the foraging and anti-predation behavior of sparrows in nature are simulated by kernel parameter λ, and the global optimal values of $\boldsymbol{\lambda}_i$ are obtained through continuous updating of sparrows' positions. Details are shown in Section 3.2.

3.2 The eugenics genetic sparrow search algorithm

Similar to other population optimization algorithms, inspired by sparrow population activities, researchers established a discoverer-follower model by simulating their foraging process and added a monitoring and early warning mechanism, the so-called sparrow search algorithm [42-45]. However, when the algorithm starts to iterate, the discoverers will approach the global optimal value, which greatly reduces the search scope of the algorithm and limits the optimization effect. Therefore, this research proposes an improved SS algorithm based on genetic thought.

Based on the traditional SS algorithm, the position of the discoverer is optimized by introducing the global optimal solution of the previous generation and the mean of fitness for some excellent individuals (eugenics). In analogy with the genetic algorithm, by assigning the good genes from the parent to the offspring, the search range of the discoverer will be significantly increased, effectively avoiding the effect of falling into local optimization. The optimized position update method is shown in Eq. (16).

$$X_{i,j}^{t+1} = \begin{cases} X_{i,j}^{t} \cdot \left(f_{j,g}^{t} - X_{j,a}^{t}\right) \cdot W & R_2 < ST \\ X_{i,j}^{t} + Q & R_2 \geq ST \end{cases} \tag{16}$$

In Eq. (16), t is the current number of iterations, $X_{i,j}^{t+1}$ is the fitness value of the i_{th} sparrow in the j_{th} dimension of the next generation, $f_{j,g}^{t}$ is the global optimal solution obtained by iteration in the j_{th} dimension of the current generation, $X_{j,a}^{t}$ is the mean fitness of the selected individuals of current generation. W is a random number of [-1,1], and Q is a random number subject to normal distribution. R_2 and ST ($R_2, ST \in [0,1]$) are early warning value and safety value respectively, which means that when the early warning value of the sparrow is below the safety value ($R_2 < ST$), the discoverer can conduct extensive search operations. When the early warning value is higher than the safety value ($R_2 \geq ST$), the sparrow will alert other sparrows and move to a safe position.

The number of sparrows responsible for vigilance generally accounts for 10%~20% of the population,

and their initial positions are randomly generated in the population. The position update of this part of the sparrow will affect the optimization range of the algorithm, so the improved position update method is shown in Eq. (17).

$$X_{i,j}^{t+1} = \begin{cases} X_{best}^{t} + \beta \cdot \left(X_{i,j}^{t} - X_{best}^{t}\right) & if\ f_i \neq f_g \\ X_{i,j}^{t} + \beta \cdot (X_{worst}^{t} - X_{best}^{t}) & if\ f_i = f_g \end{cases} \tag{17}$$

In Eq. (17), when $f_i = f_g$, the sparrow in the middle of the population has realized the danger and moved closer to other sparrows. If the sparrow is in the best position, it will be randomly adjusted to a position between the worst position. If not, no position change is made. When $f_i \neq f_g$, its position will be updated to a random position except the worst position.

3.3 Converged architecture for the SOH estimation

ML-ELM is a multi-layer neural network formed by stacking multiple ELM-AEs. Compared to deep learning networks, ML-ELM requires no fine-tuning, and has the advantages of fast training speed and high efficiency in feature information extraction. Therefore, the introduction of the EGSS-ML-KELM algorithm into the SOH estimation model can not only quickly complete the training process with fixed kernel parameters, but also enhance the robustness of the system while ensuring the prediction accuracy. The entire process is roughly divided into three components: data processing and fusion feature construction; EGSS algorithm is iteratively updated to obtain the optimal kernel function parameter values and construct the optimal model architecture; train the model to achieve SOH estimation. The SOH estimation framework for multi-algorithm synthesis is shown in Fig. 5.

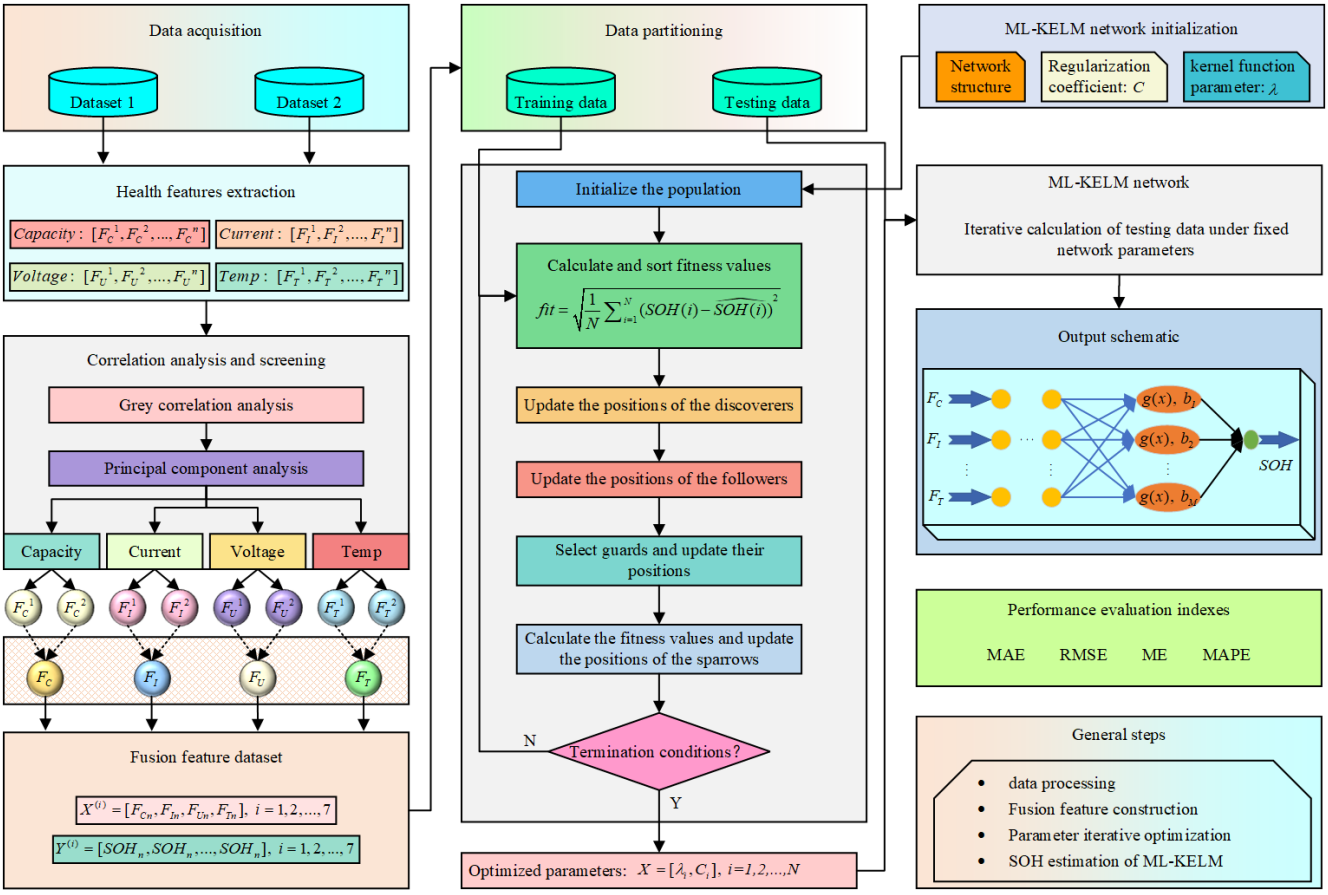

Fig. 5 SOH estimation framework

In Fig. 5, multidimensional health features are extracted from two datasets, and gray correlation analysis and principal component analysis are used to sort and screen out features that contain duplicate information. According to the correlation, the residual features are weighted and fused within the four factors of capacity, current, voltage, and temperature to obtain a 4-dimensional fusion feature dataset and perform data partitioning. After initializing the ML-KELM network and the EGSS algorithm, the RMSE of the prediction result is used as the fitness function of the EGSS algorithm, and the iteration and update of parameter optimization are started until the optimal kernel function parameter λ_i and regularization coefficient C_i for each ELM-AE are obtained. Assign the optimal parameters to the initial ML-KELM network, and use multiple evaluation indicators to test the accuracy of the optimized network on the test dataset to complete the SOH estimation process.

3.4 Evaluation metrics

In order to better evaluate the performance of the algorithm, the experimental results are further calculated and analyzed by the following three indicators.

(1) Maximum Error (ME)

$$ME = \max(\left|SOH_{true} - SOH_{predict}\right|) \tag{18}$$

(2) Mean Absolute Error (MAE)

$$MAE = \frac{1}{N}\sum_{i=1}^{N}\left|SOH_{true} - SOH_{predict}\right| \tag{19}$$

(3) Root Mean Square Error (RMSE)

$$RMSE = \sqrt{\frac{1}{N}\sum_{i=1}^{N}(SOH_{true} - SOH_{predict})^2} \tag{20}$$

(4) Mean Absolute Percentage Error (MAPE)

$$MAPE = \frac{1}{N}\sum_{i=1}^{N}\left|\frac{SOH_{true} - SOH_{predict}}{SOH_{true}}\right| \times 100\% \tag{21}$$

In the equations above, N denotes the number of samples, SOH_{true} represents the true value of SOH, $SOH_{predict}$ indicates the prediction value of SOH. In the subsequent verification and analysis section, the SOH prediction performance of each version of the ML-ELM algorithm is evaluated using the above four criteria.

4. Results and discussion

4.1 Hyper-parameter design of EGSS-ML-KELM network

After determining the estimation framework of SOH, it is necessary to set the parameters of ML-KELM network and EGSS algorithm to meet the high-precision SOH estimation of LIBs. For ML-KELM network, excessive number of hidden layers can lead to significant increases in computing costs, while conversely, it can cause significant estimation errors. For EGSS algorithm, the selection of population size and iteration times has a particularly significant impact on the optimal solution.

Excessive population size or iterations can lead to significant computational burden and time loss, although this may slightly improve the ability to optimize parameters.

The setting of all parameters does not traverse all possible values, but rather is roughly set to make the prediction result within an acceptable accuracy range. After a series of attempts, considering the impact of data volume, and balancing computational accuracy and efficiency, the setting of each parameter is shown in Tab. 5.

Tab. 5 Parameters of the algorithm

Algorithm	Parameters	Values
ML-KELM	Kernel function	RBF
	Number of hidden layers	$N = \{6, 8, 10, 12, 15\}$
EGSS	The population size	$P = \{30, 40, 60, 80\}$
	The maximum number of iterations	$T_{iteration} = \{300, 400, 500\}$
	The initial proportion of discoverers	20%
	The proportion of guards	20%
	The alert value	0.8
	The proportion of eugenic individuals	10%

The parameter settings for each test are roughly adjusted within the range given in Tab. 5. The algorithm verifications are conducted using MATLAB 2019b running on a computer with 3.2GHz AMD R7-5800H CPU and 16GB RAM.

4.2 SOH estimation with EGSS-ML-KELM network

The life-cycle data of LIBs in public datasets 1 and 2 are used to validate the model in Section 3.1. The first 90 life cycles (168 cycles in total) of each LIB in dataset 1 and the first 500 life cycles (800 cycles in total) of each LIB in dataset 2 are used as training data, and the remaining life cycles are used

for testing. The SOH estimation results of different versions of ML-ELM under the input of health features and fusion features are shown in Fig. 6.

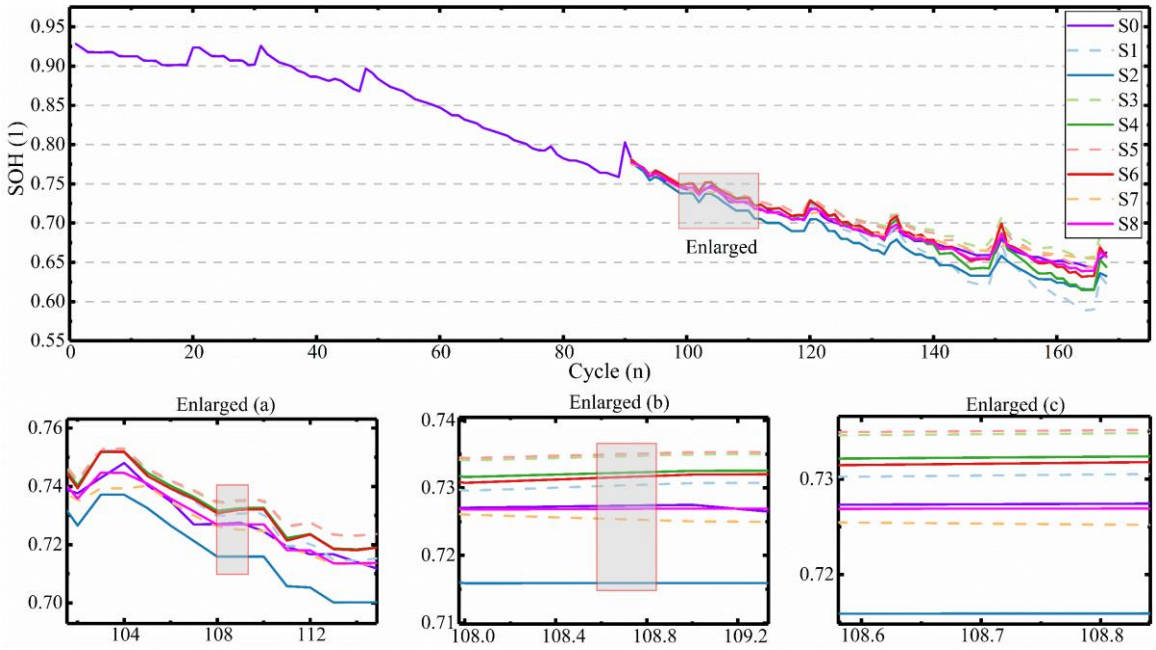

(a-1) SOH estimation results of LIB1

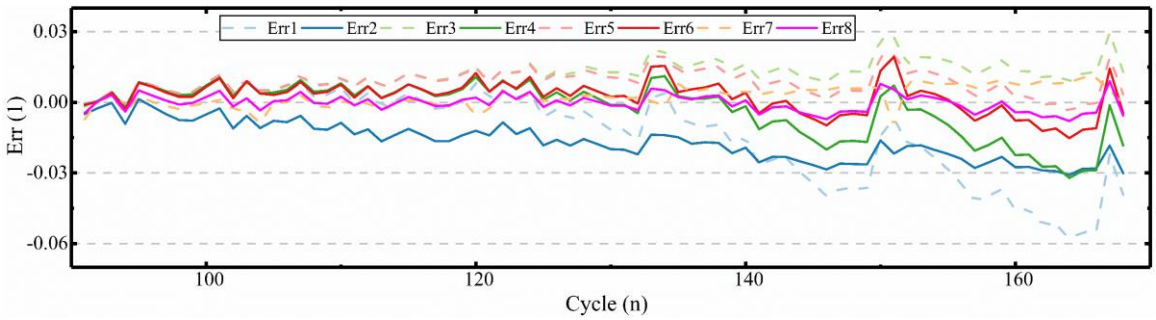

(a-2) SOH estimation errors of LIB1

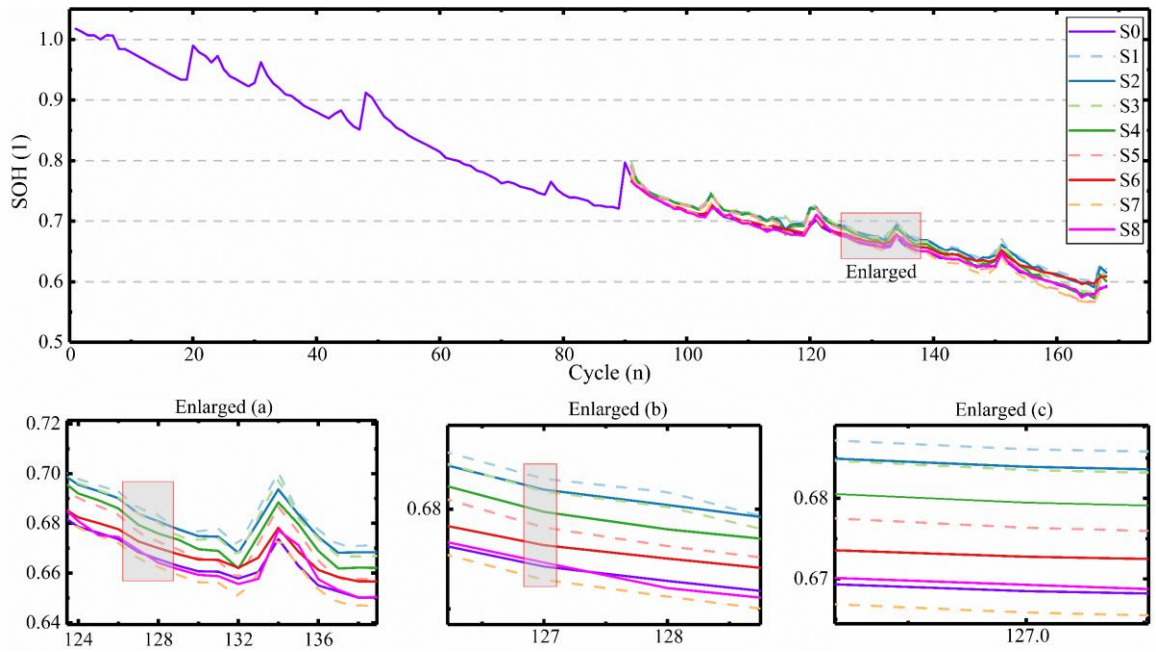

(b-1) SOH estimation results of LIB2

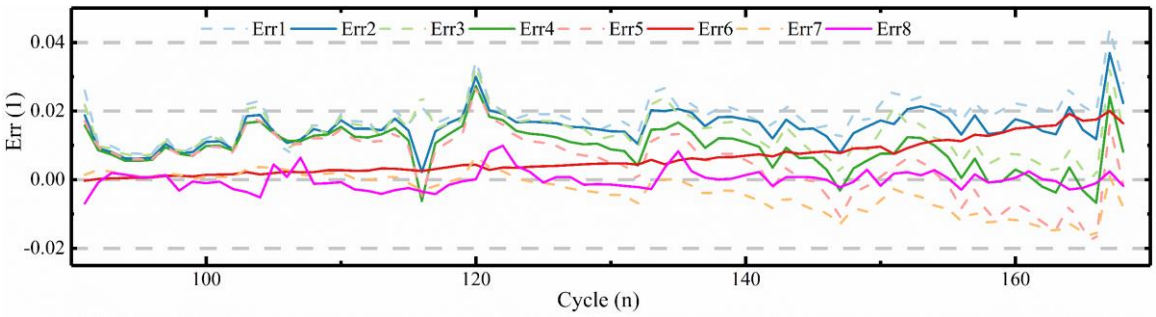

(b-2) SOH estimation errors of LIB2

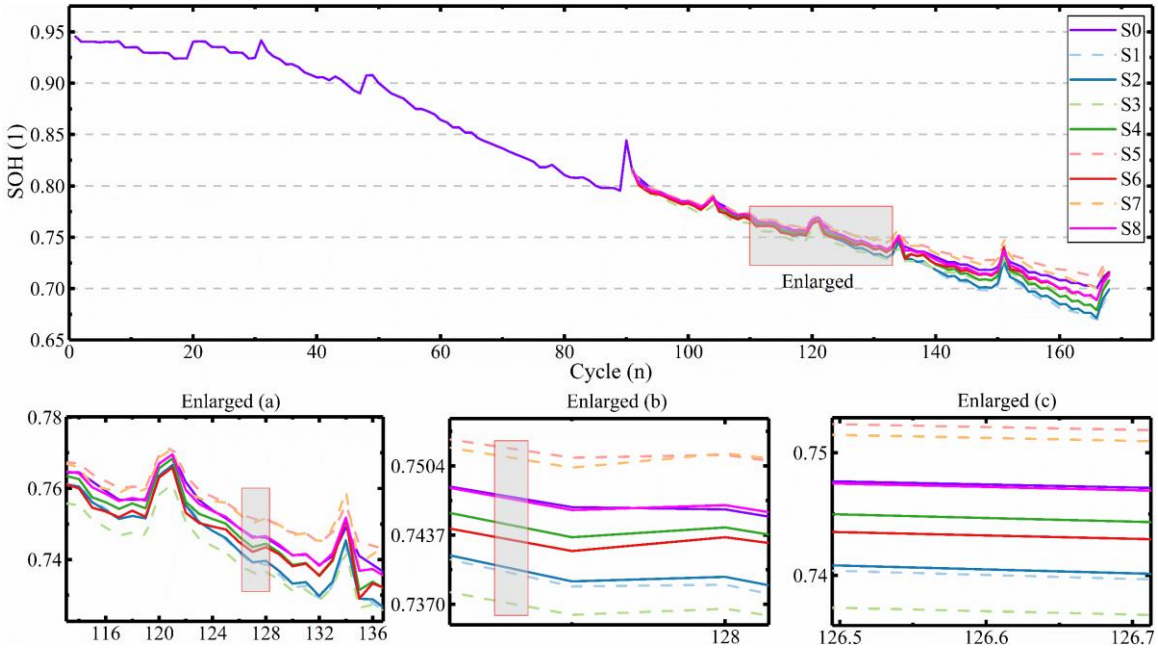

(c-1) SOH estimation results of LIB3

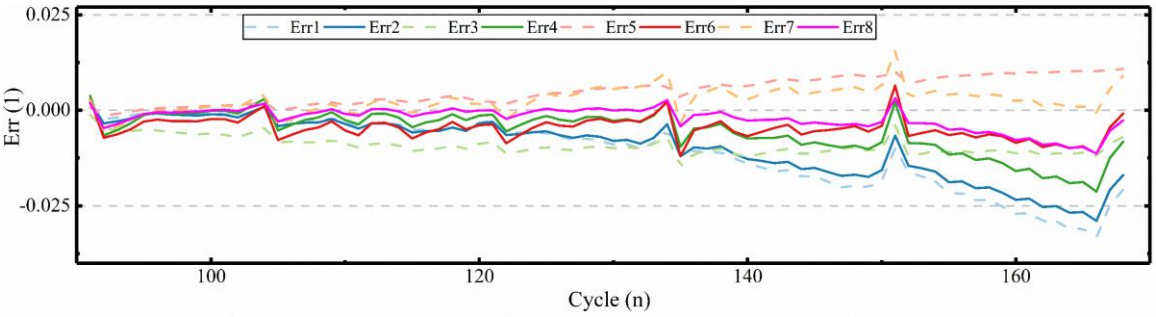

(c-2) SOH estimation errors of LIB3

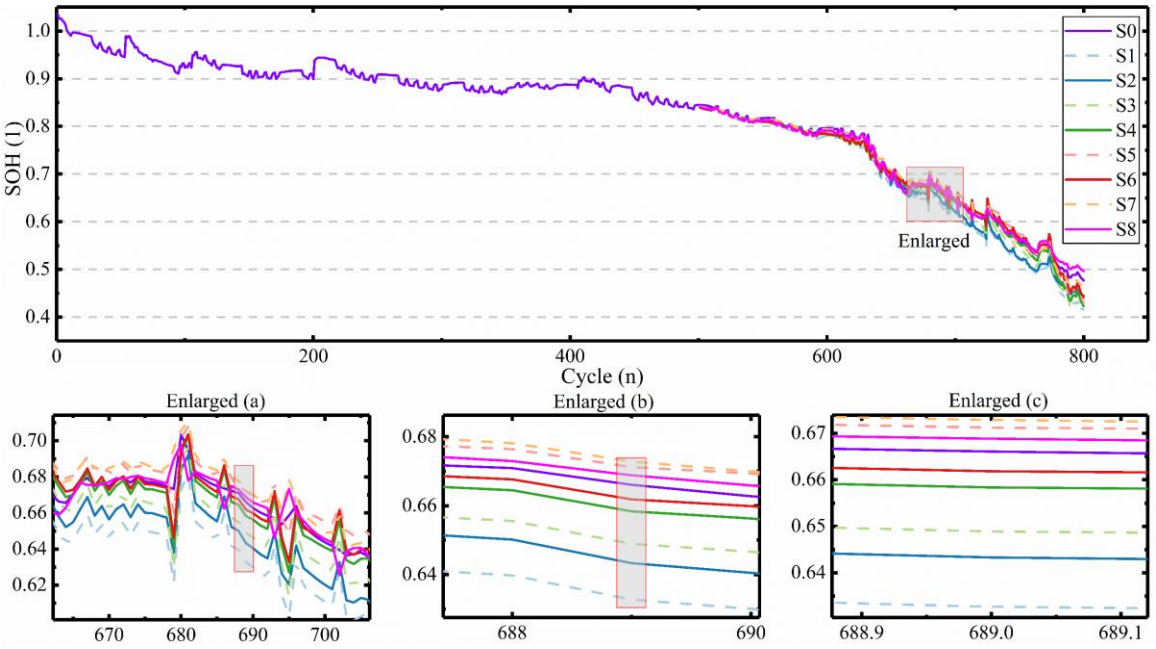

(d-1) SOH estimation results of LIB4

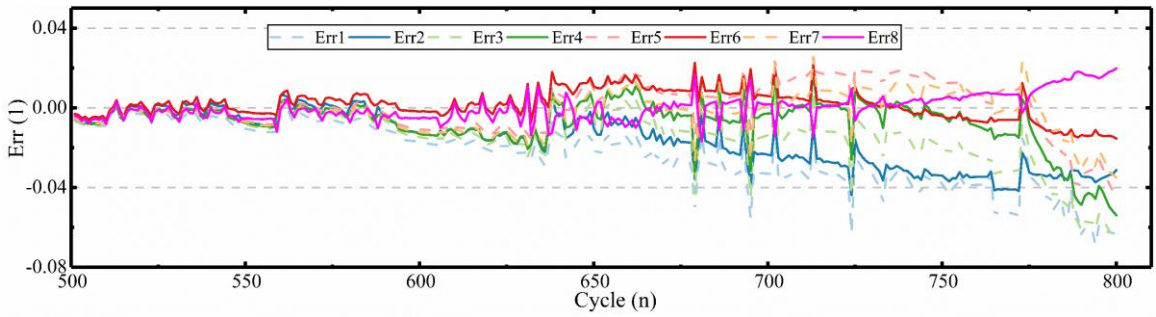

(d-2) SOH estimation errors of LIB4

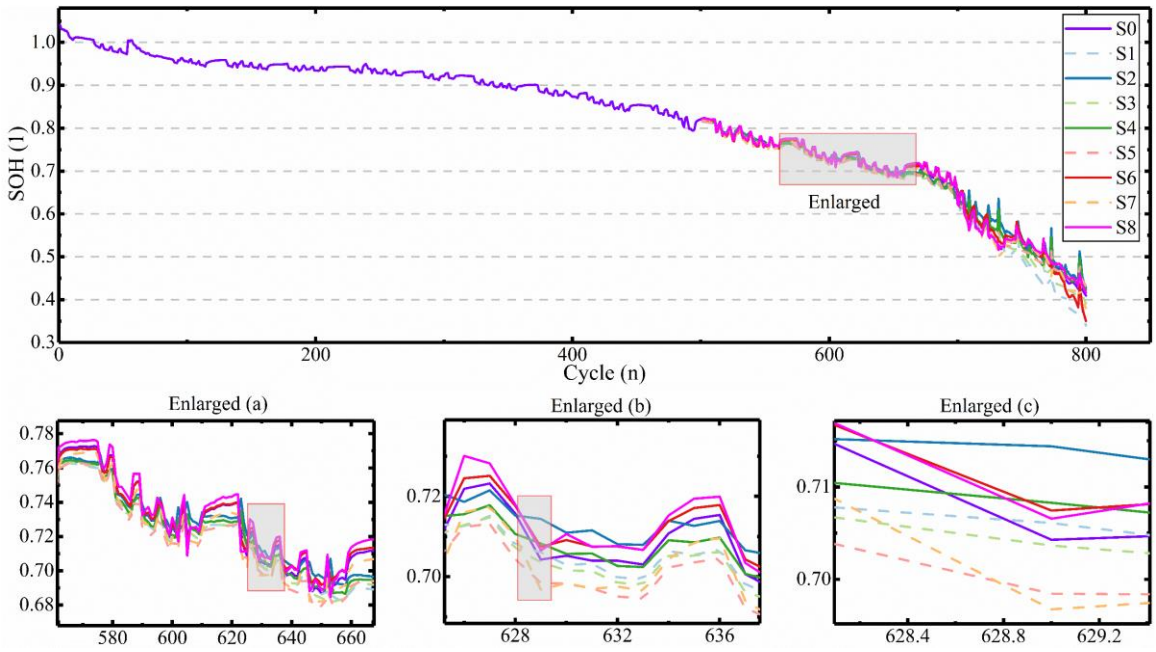

(e-1) SOH estimation results of LIB5

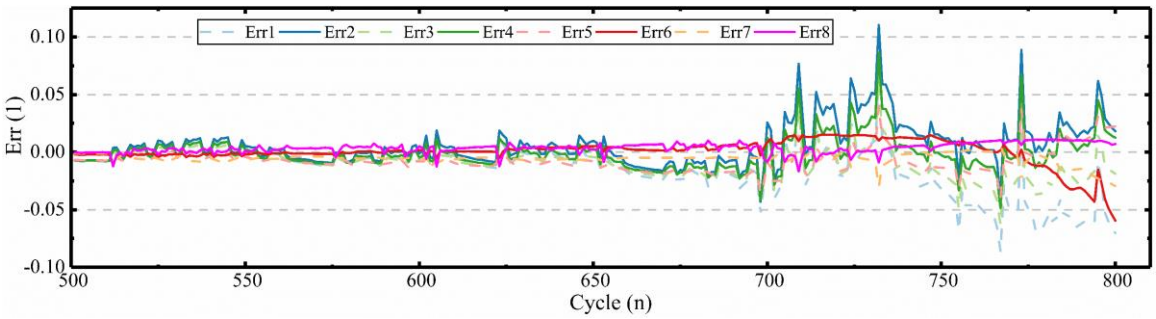

(e-2) SOH estimation errors of LIB5

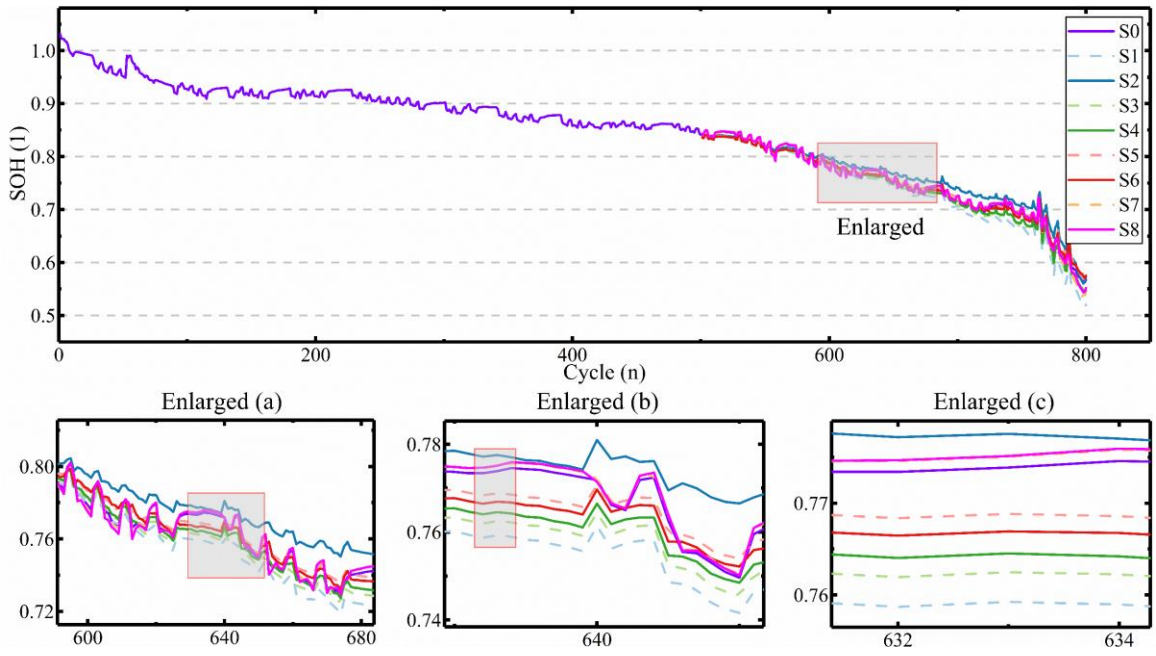

(f-1) SOH estimation results of LIB6

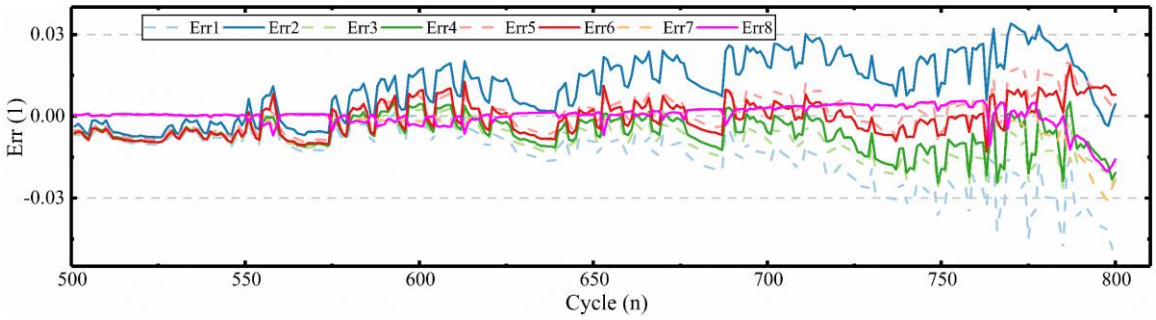

(f-2) SOH estimation errors of LIB6

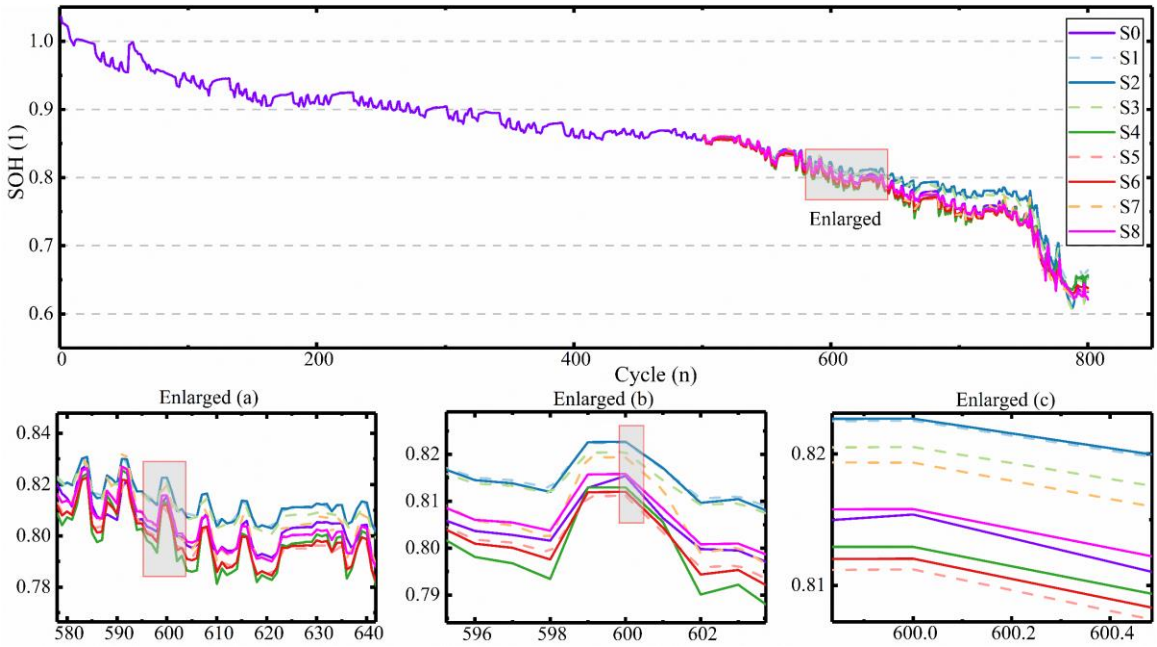

(g-1) SOH estimation results of LIB7

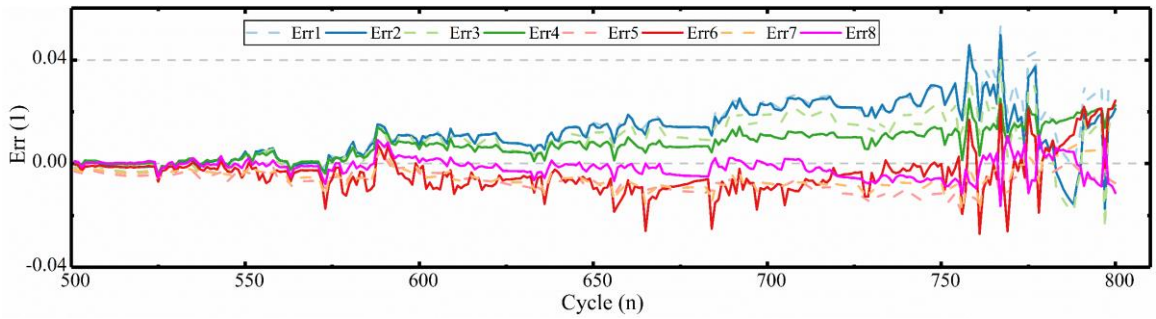

(g-2) SOH estimation errors of LIB7

Fig. 6 SOH estimation results for LIBs

In Fig. 6, S0 denotes the reference value, S1, S3, S5, and S7 denote the prediction values of ML-ELM, ML-KELM, SS-ML-KELM, and EGSS-ML-KELM algorithms under traditional health feature, and S2,

S4, S6, and S8 denote the prediction values of these algorithms under fusion features, respectively. It can be observed that ML-ELM network with kernel functions have better tracking ability and accuracy advantages for SOH estimation of LIBs. After optimizing the kernel function parameters, the accuracy advantages of SS-ML-KELM and EGSS-ML-KELM are further enhanced. In addition, each version of the ML-ELM network has better performance in fusion features compared to traditional health features as input of the network.

4.3 Model reliability evaluation

To further evaluate the SOH tracking performance of each curve in Fig. 6 for the LIB, the four criteria in Section 3.4 are applied to analyze the advantages of each version of the ML-ELM network, and the comparison results of the evaluation metrics under different specifications of the LIB cycle data are shown in Tab. 6.

Tab. 6 Reliability assessment of models

LIB cycle data		**ME**				**MAE**			
		ML-ELM	**ML-KELM**	**SS-ML-KELM**	**EGSS-ML-KELM**	**ML-ELM**	**ML-KELM**	**SS-ML-KELM**	**EGSS-ML-KELM**
LIB1	HF	0.0578	0.0296	0.0201	0.0106	0.0160	0.0120	0.0087	0.0041
	FF	0.0308	0.0321	0.0193	0.0090	0.0166	0.0086	0.0060	0.0029
LIB2	HF	0.0439	0.0330	0.0272	0.0166	0.0183	0.0134	0.0090	0.0047
	FF	0.0369	0.0273	0.0200	0.0099	0.0153	0.0098	0.0063	0.0021
LIB3	HF	0.0333	0.0146	0.0108	0.0156	0.0109	0.0092	0.0052	0.0035
	FF	0.0290	0.0213	0.0120	0.0114	0.0098	0.0059	0.0050	0.0025
LIB4	HF	0.0688	0.0642	0.0470	0.0349	0.0236	0.0143	0.0100	0.0058
	FF	0.0438	0.0539	0.0225	0.0198	0.0166	0.0089	0.0078	0.0051

LIB5	HF	0.1104	0.0630	0.0407	0.0303	0.0180	0.0125	0.0106	0.0059
	FF	0.0862	0.0860	0.0596	0.0167	0.0127	0.0099	0.0066	0.0046
LIB6	HF	0.0490	0.0268	0.0212	0.0307	0.0148	0.0093	0.0057	0.0029
	FF	0.0340	0.0246	0.0187	0.0202	0.0131	0.0070	0.0055	0.0026
LIB7	HF	0.0531	0.0400	0.0194	0.0184	0.0137	0.0101	0.0070	0.0038
	FF	0.0496	0.0250	0.0271	0.0164	0.0127	0.0067	0.0061	0.0029

LIB cycle data		**RMSE**				**MAPE**			
		ML-ELM	**ML-KELM**	**SS-ML-KELM**	**EGSS-ML-KELM**	**ML-ELM**	**ML-KELM**	**SS-ML-KELM**	**EGSS-ML-KELM**
LIB1	HF	0.0229	0.0132	0.0100	0.0051	0.0244	0.0175	0.0125	0.0060
	FF	0.0184	0.0115	0.0072	0.0036	0.0240	0.0128	0.0087	0.0042
LIB2	HF	0.0193	0.0147	0.0103	0.0064	0.0280	0.0200	0.0134	0.0075
	FF	0.0161	0.0111	0.0081	0.0029	0.0234	0.0146	0.0101	0.0032
LIB3	HF	0.0143	0.0095	0.0062	0.0043	0.0151	0.0124	0.0071	0.0047
	FF	0.0125	0.0079	0.0055	0.0037	0.0135	0.0081	0.0068	0.0035
LIB4	HF	0.0285	0.0198	0.0128	0.0074	0.0384	0.0238	0.0162	0.0091
	FF	0.0208	0.0137	0.0103	0.0066	0.0273	0.0145	0.0122	0.0080
LIB5	HF	0.0258	0.0163	0.0126	0.0076	0.0325	0.0215	0.0171	0.0098
	FF	0.0194	0.0143	0.0110	0.0056	0.0220	0.0164	0.0124	0.0078
LIB6	HF	0.0181	0.0110	0.0068	0.0056	0.0211	0.0129	0.0079	0.0044
	FF	0.0157	0.0088	0.0063	0.0041	0.0184	0.0097	0.0074	0.0038
LIB7	HF	0.0172	0.0124	0.0078	0.0055	0.0185	0.0135	0.0091	0.0050
	FF	0.0159	0.0086	0.0068	0.0040	0.0171	0.0090	0.0079	0.0040

Tab. 6. summarizes the results of the numerical evaluation of the SOH prediction performance of the ML-ELM, ML-KELM, SS-ML-KELM, and EGSS-ML-KELM on different specifications of LIB cycle data. The results show that the kernel version of ML-ELM optimized by EGSS algorithm has advantages such as high accuracy and strong robustness on each LIB compared with other versions of ML-ELM. With health features as input, the maximum values of ME, MAE, RMSE and MAPE for ML-ELM are 11.04%, 2.36%, 2.85% and 3.84%, respectively, while the maximum values of EGSS-ML-KELM for the four metrics are 3.49%, 0.59%, 0.76% and 0.98%, respectively. By replacing health features with fusion features, the maximum values for the four metrics of ML-ELM are 8.62%, 1.66%, 2.08%, and 2.73%, respectively, while those of EGSS-ML-KELM are 2.02%, 0.51%, 0.66%, and 0.80%, respectively. Obviously, regardless of which version of ML-ELM, when fusion features are used as input, the values of the four metrics significantly decrease, which means that fusion features can effectively improve the degradation of model performance caused by high-dimensional health features as input, while retaining the valid information of the original features.

To more visually demonstrate the ability of different versions of ML-ELM for SOH prediction, the numerical results of MAE, RMSE and MAPE metrics in Tab. 6 are shown as bar graphs in Fig. 7.

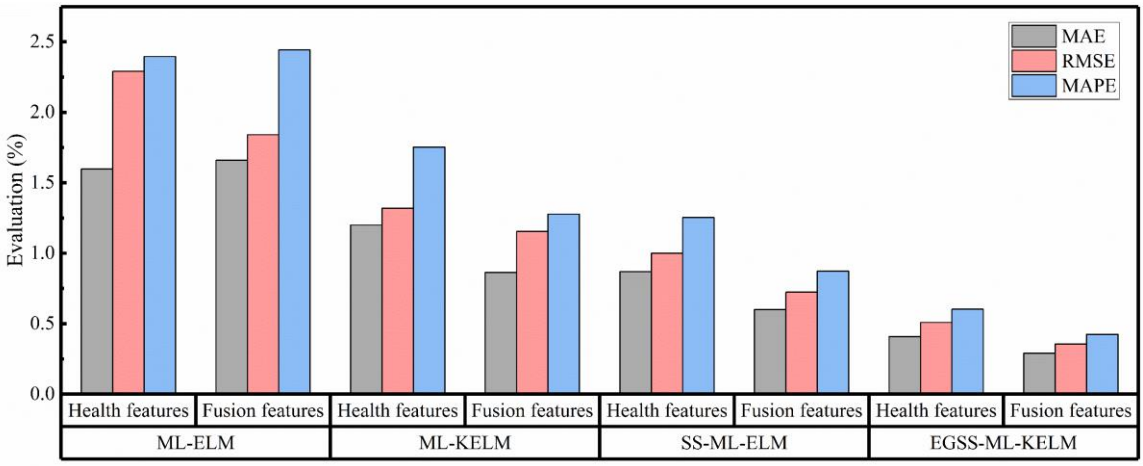

(a) Evaluation results of each algorithm for SOH estimation of LIB1

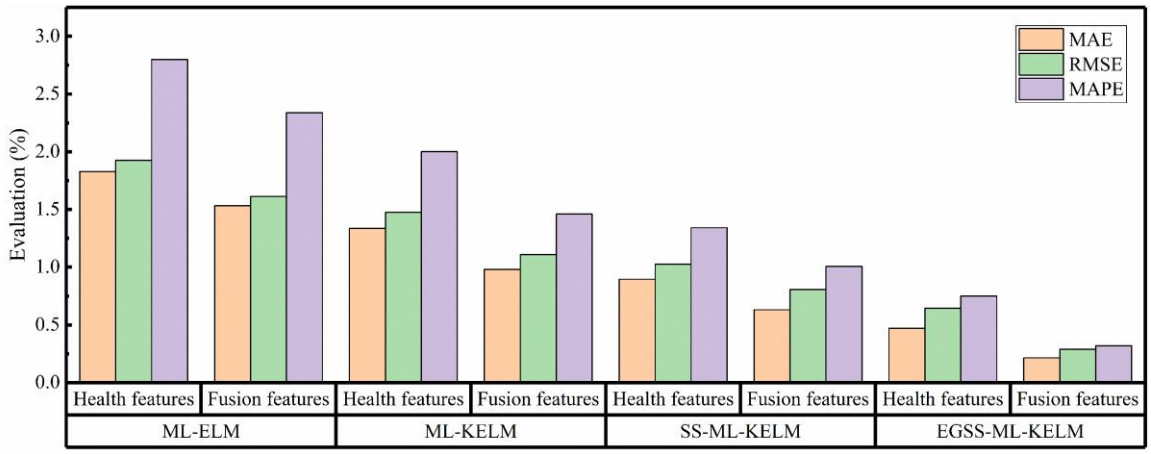

(b) Evaluation results of each algorithm for SOH estimation of LIB2

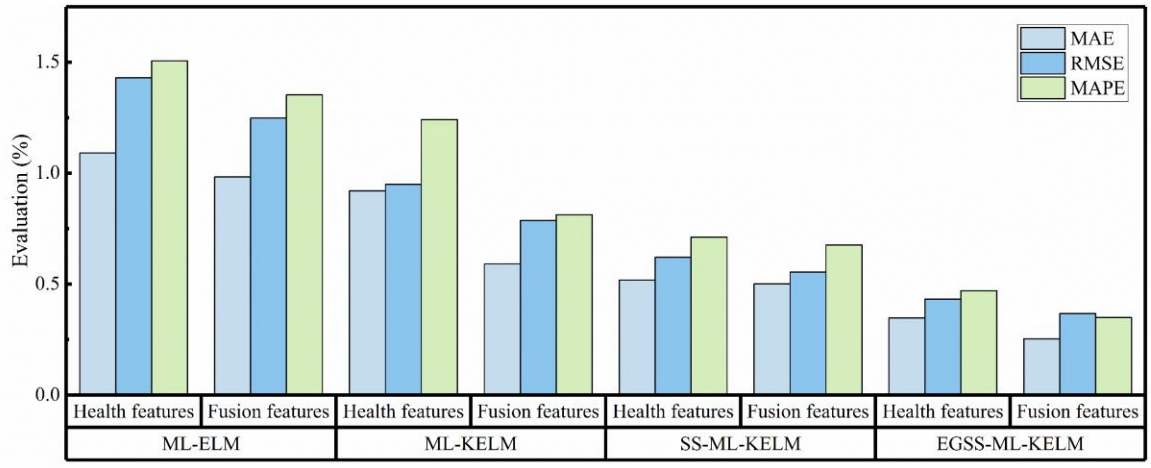

(c) Evaluation results of each algorithm for SOH estimation of LIB3

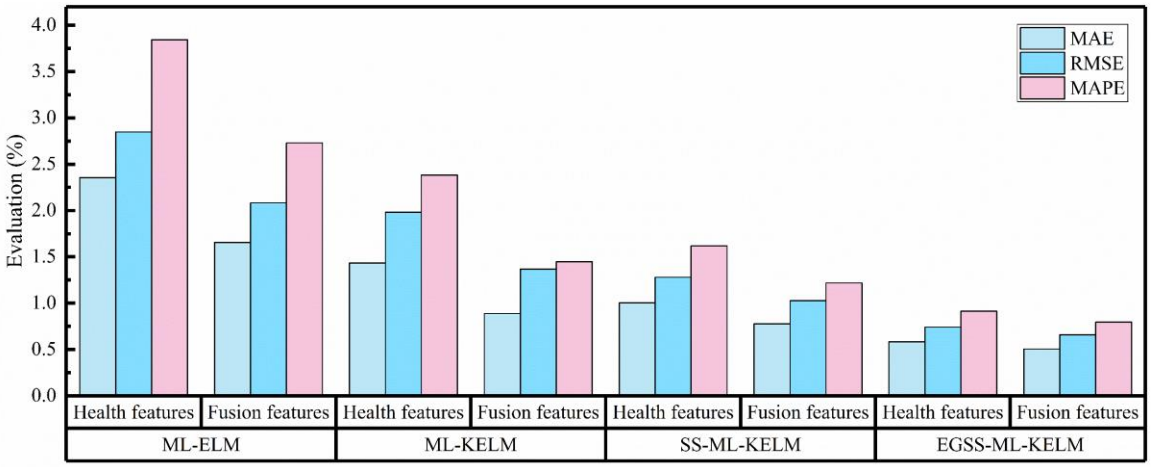

(d) Evaluation results of each algorithm for SOH estimation of LIB4

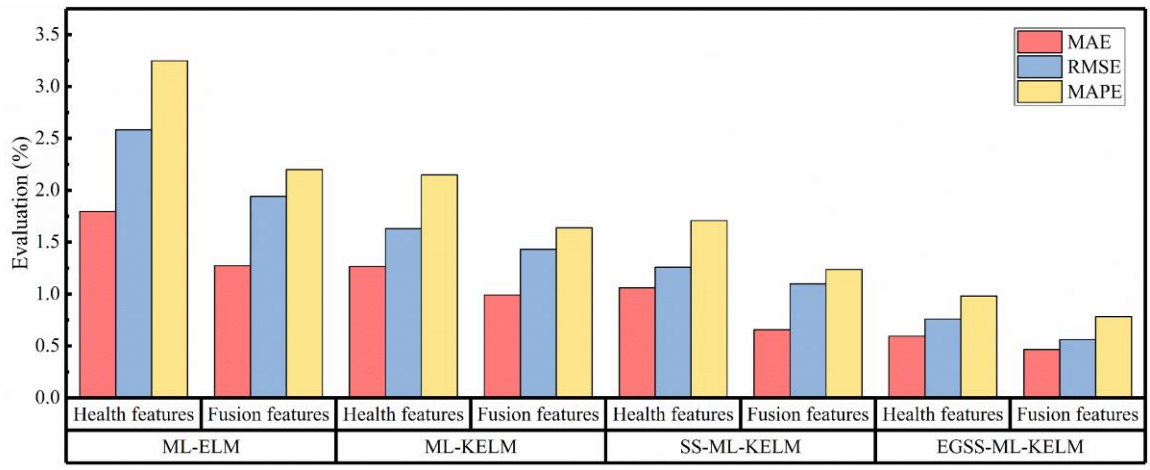

(e) Evaluation results of each algorithm for SOH estimation of LIB5

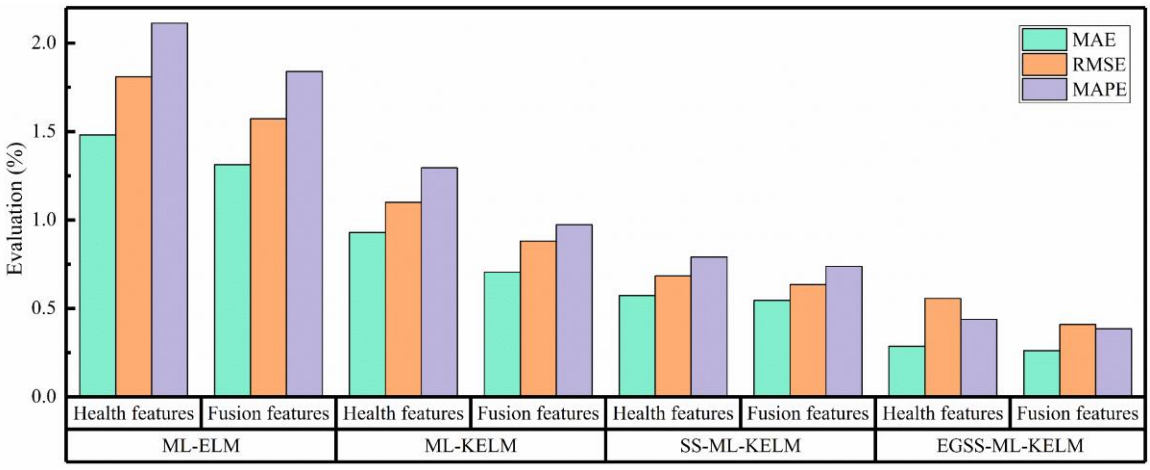

(f) Evaluation results of each algorithm for SOH estimation of LIB6

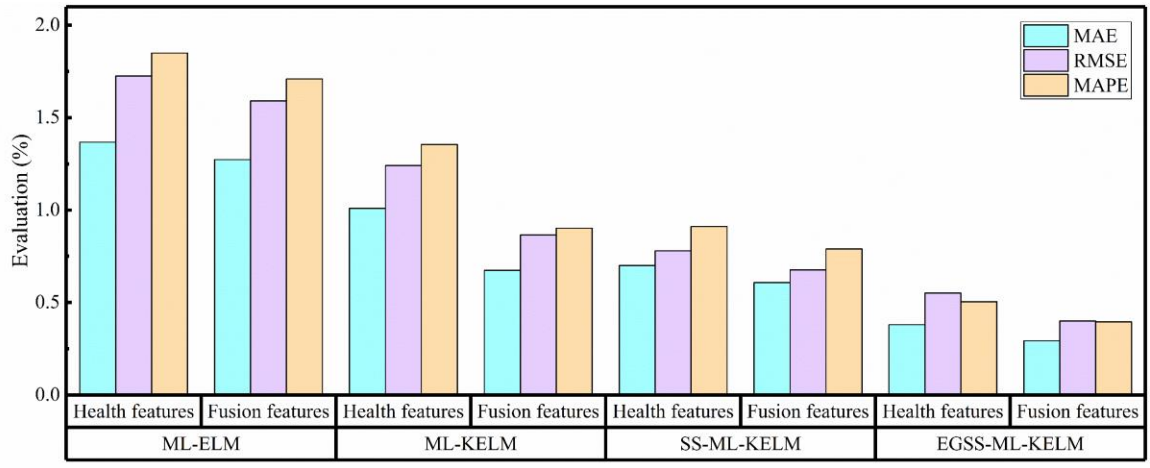

(g) Evaluation results of each algorithm for SOH estimation of LIB7

Fig. 7 Evaluation results of each algorithm for SOH estimation

Fig. 7 visualizes the results of the numerical evaluation of the three metrics, MAE, RMSE and MAPE

on the performance of each version of ML-ELM for SOH prediction in seven different specifications of LIB cycle data. Overall, compared to ML-ELM, EGSS-ML-KELM reduces the maximum values of four metrics, ME, MAE, RMSE, and MAPE, from 11.04%, 2.36%, 2.85%, and 3.84% to 3.49%, 0.59%, 0.76%, and 0.98%, respectively, demonstrating that the introduction of kernel function and EGSS algorithm are significantly effective in improving the performance of ML-ELM in SOH prediction. Under the input of low-dimensional fusion features, these indicators of EGSS-ML-ELM are 2.02%, 0.51%, 0.66%, and 0.80%, respectively, demonstrating that the fusion features not only maintain the strong tracking ability of the model, but also enhance the robustness and generality of it.

4.4 Comparative performance evaluation of the proposed EGSS-ML-KELM with other existing models

The proposed EGSS-ML-KELM model is compared with other existing SOH estimation methods using the overall best metric values to evaluate their performance. The comparison models include electrochemical impedance spectroscopy-gaussian process regression (EIS-GPR), sequential extended Kalman filter (SEKF), nonlinear auto-regressive model with exogenous inputs (NARX), active states tracking-long-short-term memory (AST-LSTM) neural network, broad learning system-long short-term memory (BLS-LSTM) neural network. The results are shown in Tab. 7.

Tab. 7 Comparison of performance between EGSS-ML-KELM model and other existing models

Models	**Battery**	**Best metric values**
EIS-GPR [46]	NCA 2.75Ah	MAE=0.725%; RMSE=0.907%
SEKF [12]	NCM 3.0Ah	ME<4%
NARX [16]	NMC 20.0Ah	MAE=0.43%; RMSE=0.46%
AST-LSTM [29]	NCA 2.0Ah	RMSE=0.38%
BLS-LSTM [41]	NCA 2.0Ah; LCO 1.35Ah	MAE=0.25%; RMSE=0.35%

EGSS-ML-KELM	NCA 2.0Ah; LCO 1.1Ah	ME=0.90%; MAE=0.21%
(Proposed in this paper)		RMSE=0.29%; MAPE=0.32%

In Tab. 7, using the same or similar battery aging data to evaluate the optimal performance of the model, it can be observed that the proposed EGSS-ML model has significant advantages in accuracy compared to other existing SOH estimation models.

5. Conclusions

This paper combines the kernel version ML-ELM network with the EGSS algorithm to propose a high-precision SOH estimation method. To solve the problems of instability and accuracy decay caused by random mapping of network parameters and the accumulation of model reconstruction errors layer by layer, a kernel learning mechanism is introduced to replace each hidden layer network with a kernel function matrix to solve the parameter setting difficulties. Compared with ML-ELM, the maximum ME, MAE, RMSE and MAPE of SOH obtained by ML-KELM individual are reduced by 4.62%, 0.93%, 0.87% and 1.46%, respectively, which strongly demonstrates the effectiveness of kernel version of ML-ELM modeling. Aiming to further improve the prediction accuracy of SOH and increase the parameter optimization range, the SS algorithm is optimized by introducing the global optimal solution of the previous generation and the individual mean value with high fitness value to complete the optimization of the kernel function parameters and realize the high accuracy and stable prediction of SOH by the system under fixed parameters. The cycle data from seven LIB units with different specification parameters are divided for model training and testing, and the health features are fused to reduce the data dimensionality. The results show that in the case of high-dimensional health features, the ME, MAE, RMSE, and MAPE of EGSS-ML-ELM are 3.49%, 0.59%, 0.76%, and 0.98%, respectively. However, in the case of fusion features, these indicators of EGSS-ML-ELM are 2.02%, 0.51%, 0.66%, and 0.80%, respectively. For independent ML-ELM and ML-KELM, these indicators are reduced by more than 50%.

Obviously, regardless of the version of ML-ELM, when using fusion features as input, the values of all four metrics will significantly decrease. This means that fusion features can effectively improve the model performance degradation caused by high-dimensional health features as input, while preserving the effective information of the raw features. Therefore, the EGSS-ML-KELM model proposed in this paper has strong robustness and adaptability to working conditions for real-time BMS applications in electric vehicles.

Acknowledgments

The work is supported by National Natural Science Foundation of China (No. 61801407), Sichuan Science and Technology Program (No. 2019YFG0427, 2023NSFSC1436), and Fund of Robot Technology Used for Special Environment Key Laboratory of Sichuan Province(No. 18kftk03).

References

[1]. X. Zhang, Z. Li, L. Luo, Y. Fan, Z. Du. A review on thermal management of lithium-ion batteries for electric vehicles. Energy, 2022. 238, Article 121652.

[2]. Y. Wang, X. Zhang, Z. Chen. Low temperature preheating techniques for Lithium-ion batteries: Recent advances and future challenges. Applied Energy, 2022. 313, Article 118832.

[3]. M. S. H. Lipu, M. A. Hannan, T. F. Karim, A. Hussain, M. H. M. Saad, A. Ayob, M. S. Miah, T. M. I. Mahlia. Intelligent algorithms and control strategies for battery management system in electric vehicles: Progress, challenges and future outlook. Journal of Cleaner Production, 2021. 292, Article 126044.

[4]. L. Song, Y. Zheng, Z. Xiao, C. Wang, T. Long. Review on Thermal Runaway of Lithium-Ion Batteries for Electric Vehicles. Journal of Electronic Materials, 2022. 51(1): pp. 30-46,

[5]. W. Zichen, D. Changqing. A comprehensive review on thermal management systems for power lithium-ion batteries. Renewable & Sustainable Energy Reviews, 2021. 139, Article 110685.

[6]. M.-F. Ge, Y. Liu, X. Jiang, J. Liu. A review on state of health estimations and remaining useful life prognostics of lithium-ion batteries. Measurement, 2021. 174, Article 109057.

[7]. W. Xie, X. Liu, R. He, Y. Li, X. Gao, X. Li, Z. Peng, S. Feng, X. Feng, S. Yang. Challenges and opportunities toward fast-charging of lithium-ion batteries. Journal of Energy Storage, 2020. 32, Article 101837.

[8]. Y. Xie, S. Wang, G. Zhang, Y. Fan, C. Fernandez, F. Blaabjerg. Optimized multi-hidden layer long short-term memory modeling and suboptimal fading extended Kalman filtering strategies for the synthetic state of charge estimation of lithium-ion batteries. Applied Energy, 2023. 336, Article 120866.

[9]. A. Saeed, N. Karimi, M. C. Paul. Analysis of the unsteady thermal response of a Li-ion battery pack to dynamic loads. Energy, 2021. 231, Article 120947.

[10]. Q. Zhang, Y. Shang, Y. Li, N. Cui, B. Duan, C. Zhang. A novel fractional variable-order equivalent circuit model and parameter identification of electric vehicle Li-ion batteries. Isa Transactions, 2020. 97: pp. 448-457,

[11]. P. Xu, X. Hu, B. Liu, T. Ouyang, N. Chen. Hierarchical Estimation Model of State-of-Charge and State-of-Health for Power Batteries Considering Current Rate. Ieee Transactions on Industrial Informatics, 2022. 18(9):

pp. 6150-6159,

[12]. X. Lai, W. Yi, Y. Cui, C. Qin, X. Han, T. Sun, L. Zhou, Y. Zheng. Capacity estimation of lithium-ion cells by combining model-based and data-driven methods based on a sequential extended Kalman filter. Energy, 2021. 216, Article 119233.

[13]. J. Tian, R. Xiong, Q. Yu. Fractional-Order Model-Based Incremental Capacity Analysis for Degradation State Recognition of Lithium-Ion Batteries. Ieee Transactions on Industrial Electronics, 2019. 66(2): pp. 1576-1584,

[14]. T. Ouyang, P. Xu, J. Lu, X. Hu, B. Liu, N. Chen. Coestimation of State-of-Charge and State-of-Health for Power Batteries Based on Multithread Dynamic Optimization Method. Ieee Transactions on Industrial Electronics, 2022. 69(2): pp. 1157-1166,

[15]. X. Hu, Y. Che, X. Lin, S. Onori. Battery Health Prediction Using Fusion-Based Feature Selection and Machine Learning. Ieee Transactions on Transportation Electrification, 2021. 7(2): pp. 382-398,

[16]. S. Khaleghi, D. Karimi, S. H. Beheshti, M. S. Hosen, H. Behi, M. Berecibar, J. Van Mierlo. Online health diagnosis of lithium-ion batteries based on nonlinear autoregressive neural network. Applied Energy, 2021. 282, Article 116159.

[17]. K. Liu, Y. Shang, Q. Ouyang, W. D. Widanage. A Data-Driven Approach With Uncertainty Quantification for Predicting Future Capacities and Remaining Useful Life of Lithium-ion Battery. Ieee Transactions on Industrial Electronics, 2021. 68(4): pp. 3170-3180,

[18]. Y. Gao, K. Liu, C. Zhu, X. Zhang, D. Zhang. Co-Estimation of State-of-Charge and State-of- Health for Lithium-Ion Batteries Using an Enhanced Electrochemical Model. Ieee Transactions on Industrial Electronics, 2022. 69(3): pp. 2684-2696,

[19]. M.-K. Tran, M. Mathew, S. Janhunen, S. Panchal, K. Raahemifar, R. Fraser, M. Fowler. A comprehensive equivalent circuit model for lithium-ion batteries, incorporating the effects of state of health, state of charge, and temperature on model parameters. Journal of Energy Storage, 2021. 43, Article 103252.

[20]. Y. Xie, S. Wang, C. Fernandez, C. Yu, Y. Fan, W. Cao, X. Chen. Improved gray wolf particle filtering and high-fidelity second-order autoregressive equivalent modeling for intelligent state of charge prediction of lithium-ion batteries. International Journal of Energy Research, 2021. 45(13): pp. 19203-19214,

[21]. X. Qiu, W. Wu, S. Wang. Remaining useful life prediction of lithium-ion battery based on improved cuckoo search particle filter and a novel state of charge estimation method. Journal of Power Sources, 2020. 450, Article 227700.

[22]. J. Bi, T. Zhang, H. Yu, Y. Kang. State-of-health estimation of lithium-ion battery packs in electric vehicles based on genetic resampling particle filter. Applied Energy, 2016. 182: pp. 558-568,

[23]. H. Feng, G. Shi. SOH and RUL prediction of Li-ion batteries based on improved Gaussian process regression. Journal of Power Electronics, 2021. 21(12): pp. 1845-1854,

[24]. M. S. H. Lipu, M. A. Hannan, A. Hussain, A. Ayob, M. H. M. Saad, T. F. Karim, D. N. T. How. Data-driven state of charge estimation of lithium-ion batteries: Algorithms, implementation factors, limitations and future trends. Journal of Cleaner Production, 2020. 277, Article 124110.

[25]. Y. Song, D. Liu, H. Liao, Y. Peng. A hybrid statistical data-driven method for on-line joint state estimation of lithium-ion batteries. Applied Energy, 2020. 261, Article 114408.

[26]. Z. Cui, L. Wang, Q. Li, K. Wang. A comprehensive review on the state of charge estimation for lithium-ion battery based on neural network. International Journal of Energy Research, 2022. 46(5): pp. 5423-5440,

[27]. X. Ren, S. Liu, X. Yu, X. Dong. A method for state-of-charge estimation of lithium-ion batteries based on PSO-LSTM. Energy, 2021. 234, Article 121236.

[28]. M. A. Patil, P. Tagade, K. S. Hariharan, S. M. Kolake, T. Song, T. Yeo, S. Doo. A novel multistage Support Vector Machine based approach for Li ion battery remaining useful life estimation. Applied Energy, 2015. 159: pp. 285-297,

[29]. P. Li, Z. Zhang, Q. Xiong, B. Ding, J. Hou, D. Luo, Y. Rong, S. Li. State-of-health estimation and remaining

useful life prediction for the lithium-ion battery based on a variant long short term memory neural network. Journal of Power Sources, 2020. 459, Article 228069.

[30]. L. Chen, Y. Ding, H. Wang, Y. Wang, B. Liu, S. Wu, H. Li, H. Pan. Online Estimating State of Health of Lithium-Ion Batteries Using Hierarchical Extreme Learning Machine. Ieee Transactions on Transportation Electrification, 2022. 8(1): pp. 965-975,

[31]. L. Chen, H. Wang, B. Liu, Y. Wang, Y. Ding, H. Pan. Battery state-of-health estimation based on a metabolic extreme learning machine combining degradation state model and error compensation. Energy, 2021. 215, Article 119078.

[32]. H. Pan, Z. Lu, H. Wang, H. Wei, L. Chen. Novel battery state-of-health online estimation method using multiple health indicators and an extreme learning machine. Energy, 2018. 160: pp. 466-477,

[33]. G. Huang, G.-B. Huang, S. Song, K. You. Trends in extreme learning machines: A review. Neural Networks, 2015. 61: pp. 32-48,

[34]. Z. Deng, X. Hu, P. Li, X. Lin, X. Bian. Data-Driven Battery State of Health Estimation Based on Random Partial Charging Data. Ieee Transactions on Power Electronics, 2022. 37(5): pp. 5021-5031,

[35]. D. Roman, S. Saxena, V. Robu, M. Pecht, D. Flynn. Machine learning pipeline for battery state-of-health estimation. Nature Machine Intelligence, 2021. 3(5): pp. 447-456,

[36]. J. Li, X.-Y. Hou. Dynamic reconstruction of chaotic system based on exponential weighted online sequential extreme learning machine with kernel. Acta Physica Sinica, 2019. 68(10), Article 100503.

[37]. Y. Liu, J. Wang. Transfer learning based multi-layer extreme learning machine for probabilistic wind power forecasting. Applied Energy, 2022. 312, Article 118729.

[38]. P. Ding, X. Liu, H. Li, Z. Huang, K. Zhang, L. Shao, O. Abedinia. Useful life prediction based on wavelet packet decomposition and two-dimensional convolutional neural network for lithium-ion batteries. Renewable & Sustainable Energy Reviews, 2021. 148, Article 111287.

[39]. J. Yu. State of health prediction of lithium-ion batteries: Multiscale logic regression and Gaussian process regression ensemble. Reliability Engineering & System Safety, 2018. 174: pp. 82-95,

[40]. Y. Cui, Y. Chen. Prognostics of Lithium-Ion Batteries Based on Capacity Regeneration Analysis and Long Short-Term Memory Network. Ieee Transactions on Instrumentation and Measurement, 2022. 71, Article 2511613.

[41]. S. Zhao, C. Zhang, Y. Wang. Lithium-ion battery capacity and remaining useful life prediction using board learning system and long short-term memory neural network. Journal of Energy Storage, 2022. 52, Article 104901.

[42]. J. Xue, B. Shen. A novel swarm intelligence optimization approach: sparrow search algorithm. Systems Science & Control Engineering, 2020. 8(1): pp. 22-34,

[43]. G. Liu, C. Shu, Z. Liang, B. Peng, L. Cheng. A Modified Sparrow Search Algorithm with Application in 3d Route Planning for UAV. Sensors, 2021. 21(4), Article 1224.

[44]. C. Zhang, S. Ding. A stochastic configuration network based on chaotic sparrow search algorithm. Knowledge-Based Systems, 2021. 220,

[45]. Y. Zhu, N. Yousefi. Optimal parameter identification of PEMFC stacks using Adaptive Sparrow Search Algorithm. International Journal of Hydrogen Energy, 2021. 46(14): pp. 9541-9552,

[46]. B. Jiang, J. Zhu, X. Wang, X. Wei, W. Shang, H. Dai. A comparative study of different features extracted from electrochemical impedance spectroscopy in state of health estimation for lithium-ion batteries. Applied Energy, 2022. 322, Article 119502.